

Contents lists available at ScienceDirect

Petroleum Science

journal homepage: www.keaipublishing.com/en/journals/petroleum-science



Original Paper

Investigation into the characteristics of magnesite tailings-catalyzed gasification of petroleum coke



Xian-Chao Du^{a,1}, Xiang Liu^{a,1}, Qian-Yun Liu^a, Bing Wang^{b,*}

- ^a College of Chemistry and Pharmaceutical Engineering, Nanyang Normal University, Nanyang, 473061, Henan, China
- b School of Electric Power, Civil Engineering and Architecture, Shanxi University, Taiyuan, 030006, Shanxi, China

ARTICLE INFO

Article history: Received 28 September 2024 Received in revised form 23 April 2025 Accepted 14 August 2025 Available online 21 August 2025

Edited by Min Li

Keywords:
Petroleum coke
Catalytic gasification
Mg-based tailings
Carbon microstructure
Kinetics

ABSTRACT

This study systematically investigated the catalytic gasification of two distinct petroleum coke (PC) using magnesium-based tailings (MT) as the catalyst. The research objectives focused on comparative analysis of gasification reactivities and elucidation of carbon microstructure evolution during PC gasification. Experimental results demonstrate that PC-B (derived from Liaohe Oilfields delayed coking) exhibited significantly higher gasification activity than PC-A (from Karamay Oilfields delayed coking), with aromatic C-H content and polycondensation index showing stronger correlations with reactivity than graphitization parameters. Notably, the MT catalyst exhibited material-dependent catalytic behaviors during gasification. MT catalyst enhanced structural ordering in PC-B by: (i) developing denser aromatic carbon layers, (ii) improving microcrystalline alignment, and (iii) elevating graphitization degree. These structural modifications contrasted sharply with PC-A's response, where MT introduction generated active MgO species in the ash phase, boosting gasification reactivity. Conversely, in PC-B ash systems, MgO preferentially reacted with Al_2O_3 to form inert MgAl $_2O_4$ spinel, effectively deactivating the catalyst. Kinetic investigations validated the shrinking core model (SCM) as the dominant mechanism, with calculated activation energies of 172.12 kJ/mol (PC-A + 5% MT) and 137.19 kJ/mol (PC-B + 5% MT).

© 2025 The Authors. Publishing services by Elsevier B.V. on behalf of KeAi Communications Co. Ltd. This is an open access article under the CC BY-NC-ND license (http://creativecommons.org/licenses/by-nc-nd/4.0/).

1. Introduction

The global escalation in industrial activities has led to a significant increase in crude oil consumption, consequently escalating PC production volumes. This trend is further intensified by the declining quality of crude oil sources, leading to an increased output of high-sulfur PC (Yu et al., 2020; Wu et al., 2018). PC remains an attractive fuel source for power generation facilities due to its beneficial properties: high calorific value, rich carbon content, and low ash content (Wei et al., 2017). Nevertheless, the environmental liabilities associated with PC utilization cannot be overlooked. The high sulfur content in PC contributes directly to sulfur oxide (SO_X) emissions, posing severe ecological threats.

E-mail address: wangbing@sxu.edu.cn (B. Wang).

Peer review under the responsibility of China University of Petroleum (Beijing).

¹ These authors contributed equally to this work.

Consequently, there is an urgent need to develop and implement strategies that not only efficiently harness the energy potential of PC but also mitigate its detrimental environmental impacts. Advancing towards more sustainable utilization of this resource is critical for balancing economic benefits with environmental protection.

Gasification offers substantial potential for converting solid fuels into a diverse range of chemical commodities through the syngas pathway. This not only boosts the efficiency of solid fuel utilization but also mitigates environmental pollution, thereby aligning with sustainability objectives (Li et al., 2018; Wang et al., 2018). However, the restricted reactivity in gasification processes poses a significant challenge, hindering the broader adoption of PC as a primary feedstock.

To address this limitation, catalytic gasification using alkali metal-based catalysts has emerged as a pivotal technological approach for enhancing solid fuel conversion efficiency. Recent advances demonstrate marked improvements in reaction rates and carbon utilization. Ouyang et al. highlighted the efficiency of K-based composite catalysts in PC gasification (Ouyang et al.,

^{*} Corresponding author.

2020), noting that KOH remarkably enhanced the carbon conversion rates. Xu et al. systematically investigated the catalytic efficacy of Na/Fe bimetallic systems (Xu et al., 2020), identifying 4 wt% Na loading as optimal for suppressing polyaromatic condensation while facilitating oxygen transfer via C–O–Na intermediates. Ban et al. delved into Ca-catalyzed steam gasification of char (Ban et al., 2019), underscoring the pivotal role of in-situ CaCO₃ decomposition in mediating the catalytic process. Furthermore, Zhou et al. examined Fe-based catalysts in biomass gasification and found that a 10% weight loading of Fe achieved peak catalytic performance (Zhou et al., 2022).

The application of alkaline metal catalysts in catalytic gasification, though promising, is accompanied by several drawbacks. These catalysts are prone to deactivation and face dual challenges: high costs and limited recoverability, which have impeded their widespread industrial adoption (Zhang et al., 2009; Liu et al., 2021; Wang et al., 2022; Gao et al., 2011; Mei et al., 2017). To address these issues, research has pivoted towards investigating and implementing the use of disposable solid waste catalysts. This shift offers multiple benefits: it enhances affordability, promotes environmental sustainability, and leverages the significant metallic content found in such wastes, making them a compelling alternative.

Zhang et al. highlighted the superior catalytic activity of black liquor compared to pure alkali metals, demonstrating a significant enhancement in the gasification reactivity of PC (Zhang et al., 2015). This finding underscores the potential of waste-derived catalysts in boosting process efficiency. Similarly, He et al. reported that the liquefied Fe-based catalysts significantly improved char gasification reactivity due to their large specific surface area and rich content of Fe and alkali and alkaline earth metal species (AAEMs) (He et al., 2022). Linghu et al. utilized blast furnace (BF) slag as a catalytic agent (Linghu et al., 2019), revealing its effectiveness in destabilizing stable C=C bonds in aromatic structures, thereby facilitating the formation of reactive C(O) compounds. Collectively, these studies illustrate the promise of exploring unconventional, eco-friendly, and economically feasible catalysts derived from waste materials. Such innovations have the potential to revolutionize the field of catalytic gasification, enhancing both its economic viability and environmental sustainability.

China is endowed with vast magnesite reserves, estimated at 3.4 billion tons, which account for 26% of the global total (Zhu et al., 2023; Dong et al., 2023). The flotation tailings, typically viewed as waste from magnesite processing, are in fact a rich source of magnesium-based compounds. These compounds possess untapped potential to enhance the catalytic gasification of PC.

The integration of Mg-based compounds into the PC gasification process could serve a dual purpose: it has the potential to enhance the efficiency of PC gasification while concurrently enabling the eco-efficient utilization of China's magnesite resources. Previous research has highlighted the significant catalytic potential of Mg-based materials in accelerating high-temperature reactions (Tian et al., 2019; Liang et al., 2019; Li et al., 2014; Alarcón et al., 2004). Liang et al. established that Mg compounds exhibited distinct catalytic performances in PC gasification (Liang 2019), with activity following the sequence: $MgCl_2 > MgO > Mg(NO_3)_2 > MgSO_4$. Their findings further identified a threshold limit for MgCl₂ additive concentration, demonstrating optimal catalytic efficacy at a 5% loading level (Tian et al., 2019). Li et al. elucidated MgO's capacity to actively supply lattice oxygen for soot oxidation catalysis (Li et al., 2014), a critical functionality maintained even under anaerobic conditions, thereby highlighting its distinct catalytic functionality in oxygendeficient environments. Furthermore, Alarcón et al. investigated the synergistic interactions between MgO and CaO in gasification systems (Alarcón et al., 2004), revealing that MgO incorporation effectively suppresses carbon deposition and inhibits bidentate carbonate formation on CaO surfaces, thereby substantially improving catalytic durability and reaction efficiency. However, present research predominantly focuses on the kinetics of PC gasification under the influence of Mg-based catalysts, with limited attention given to the structural evolutions during PC catalytic gasification process. Deciphering these structural modifications is crucial for a comprehensive evaluation of the effectiveness and mechanisms of Mg-based catalysts. Such insights are essential for informing the design of more efficient and selective catalyst formulations.

This investigation is focused on the catalytic gasification kinetics and structural evolution of PC influenced by Mg-based tailings. Utilizing isothermal gasification tests, the study aims to evaluate how these catalysts enhance PC reactivity, thereby elucidating the mechanisms responsible for improved gasification efficiency. To thoroughly explore the structural modifications induced by Mgbased catalysts, advanced analytical techniques such as X-ray Diffraction (XRD) and Fourier Transform Infrared Spectroscopy (FTIR) are employed. XRD analysis will uncover any changes in the crystalline structure of carbonaceous material, offering insights into the interactions between magnesium components and the PC lattice, as well as potential alterations to its crystallographic arrangement. FTIR spectra will reveal changes in functional groups, reflecting modifications to the PC's surface chemistry and potentially revealing insights into bonding rearrangements influenced by the catalyst. Furthermore, BET analysis will provide critical data on the pore structure and specific surface area of PC after exposure to the catalyst. These parameters are vital in determining the accessibility of reactants to the active sites and overall gasification performance. In essence, this multidimensional approach not only refines our comprehension of the catalytic action of Mg-based tailings in PC gasification but also provides innovative perspectives for optimizing PC utilization efficiency.

2. Experimental

2.1. Details of samples

Two representative PCs were procured for comparative investigation: PC-A derived from heavy high-sulfur residue oil (Liaohe Oilfield, Liaoning) and PC-B originating from light low-sulfur residue oil (Karamay Oilfield, Xinjiang). This strategic selection enables systematic evaluation of feedstock-dependent gasification behaviors. Prior to experimentation, the samples underwent standardized preparation: mechanical pulverization, sieving to $<\!74\,\mu m$ particle size, and oven-drying at 105 °C for 24 h to remove moisture.

Proximate and ultimate analyses performed in accordance with Chinese National Standards (GB/T 212-2008 and GB/T 31391-2015) are summarized in Table 1. Both PCs exhibit premium gasification potential because of their exceptionally high fixed carbon content

Table 1Proximate and ultimate analysis of samples.

Sample	Proximate analysis, wt% (ad)			Ultimate analysis, wt% (daf))	
	Ash	M	V	FC	С	Н	O ^a	N	S
PC-A PC-B	0.15 1.12	0.60 0.76	9.60 10.66	89.65 87.47	87.42 90.32			1.46 2.87	6.20 0.11

Note: ad-air dried basis; daf-dry ash free basis.

^a Determined by difference.

(>87 wt%). Additionally, PC-B has relatively higher ash and oxygen contents compared to PC-A. Table 2 presents a detailed analysis of the chemical composition of PC ash and the MT catalyst, as determined by X-ray fluorescence spectrometry (XRF). Notably, MgO accounts for an impressive 69.94 wt% in the MT catalyst. Further investigation into how these chemical components interact with PC during gasification is essential for fully realizing the potential of this waste-derived catalyst.

2.2. TG analysis and reaction kinetics

The reactivity of the PC sample during gasification was investigated using a TGA (SII TG/DTA 7300) with an isothermal gasification method. Approximately 5 mg of PC sample was loaded into an alumina crucible. The sample was heated at a controlled rate of 30 °C/min under a steady flow of high-purity N_2 gas at 100 mL/min until it reached the target temperature. Once this temperature was achieved, the carrier gas was switched from N_2 to CO_2 at a flow rate of 150 mL/min and maintained for a duration of 2 h. This procedure allowed for the assessment of the sample's reactivity and provided insights into the gasification kinetics. The carbon conversion rate (x) was determined using the following equation:

$$x = \frac{m_0 - m_t}{m_0 - m_{ash}} \tag{1}$$

where m_0 and m_{ash} represent the initial mass and final mass of PC, mg; m_t is the mass of PC residue at any given time t, mg.

2.3. FTIR analysis

The FTIR assessment of PC samples was carried out using a Bruker Tensor II spectrometer, enabling an in-depth examination of the samples' functional groups and carbon lattice structures. Spectral data was collected over a wavenumber range of $500-4000~\rm cm^{-1}$ with a resolution of $4~\rm cm^{-1}$ to ensure enhanced precision. Several key characteristics were identified, including the extent of graphitization, the ratio of C–H bonds present in aromatic rings, and the degree of aromaticity. To elucidate the carbon structure within the PC, its carbon constituents were categorized into two primary types: aromatic carbon ($C_{\rm ar}$) and aliphatic carbon ($C_{\rm al}$). Quantitative assessments of PC's carbon structure and the oxygen-containing functional groups were achieved by employing the following equations (Chen et al., 2012).

$$I_{a} = \frac{A(C=0)}{A(C=0) + A(C=C)}$$
 (2)

$$I_{b} = \frac{A(C - O)}{A_{\text{total}}} \tag{3}$$

$$I_{c} = \frac{A(C - H_{aromatic})}{A_{total}}$$
 (4)

$$I_{\rm d} = \frac{A\left(C - H_{\rm aliphatic}\right)}{A(C - H_{\rm aromatic})} \tag{5}$$

Table 2Chemical composition analysis of PC ash and MT catalyst.

$$I_{e} = \frac{A(\text{CH}_{2})}{A(\text{CH}_{3})} \tag{6}$$

where $I_{\rm a}$ denotes the degree of graphitization, $I_{\rm b}$ denotes the proportion of oxygen-containing functional groups, $I_{\rm c}$ denotes the proportion of C–H in aromatics, $I_{\rm d}$ denotes the ratio of C–H in aliphatic and aromatic, and $I_{\rm e}$ denotes the polycondensation degree.

2.4. XRD analysis

The XRD analysis of PC samples was conducted using the advanced RIGAKU D/max-rB instrument to delve into the intricate microcrystalline structure. By applying Bragg's Law, the layer plane spacing (d_{002}) was determined, providing insights into the stacking distance of the carbon layers. The Scherrer equation was utilized to estimate two pivotal features of the aromatic layers: the accumulation height (L_c) , indicative of the vertical extension of the ordered carbon stacks, and the size (L_a) , referring to the lateral dimensions or coherence length of these layers (Lu et al., 2001; Wu et al., 2017). Additionally, the number of accumulation layer (n) was calculated as the ratio of L_c to d_{002} , offering a measure of the stacking density of the aromatic microcrystallites. The crystallinity index (CrI) was adopted to qualitatively assess the degree of ordering within the aromatic layers. Higher CrI values denote a more crystalline and ordered structure.

$$d_{002} = \frac{\lambda}{2\sin(\theta_{002})}\tag{7}$$

$$L_{\rm c} = \frac{0.94\lambda}{\beta_{002} \cos(\theta_{002})} \tag{8}$$

$$L_{\rm a} = \frac{1.84\lambda}{\beta_{100}\cos(\theta_{100})}\tag{9}$$

$$n = \frac{L_{\rm c}}{d_{002}} \tag{10}$$

$$CrI = \frac{I_{002} - I_{AM}}{I_{002}} \times 100\%$$
 (11)

where the incident wavelength symbolized as λ is 1.54 nm. The angles denoted as θ_{002} and θ_{100} correspond to the glancing angles of peak (002) and peak (100) respectively, while β_{002} and β_{100} represent the full width at half maximum of peak (002) and peak (100) respectively, measured in radians. Furthermore, I_{002} and I_{AM} stand for the diffraction intensity of peak (002) and the amorphous carbon peak, respectively.

2.5. BET analysis

The analysis of the pore structure and specific surface area of the PC sample was conducted using a physical adsorption instrument, providing a detailed characterization of its microstructural properties. The specific surface area was determined using the BET theory, while further insights into the pore characteristics,

including the average pore size, total pore volume, and pore size distribution, were obtained through the BJH method. This intricate microstructure of the PC sample is crucial for understanding its properties and potential applications.

2.6. Reaction kinetic analysis

2.6.1. Random pore model (RPM)

The RPM was developed for the random distribution of nuclei in crystalline growth (Lopez-Gonzalez et al., 2014; Wang et al., 2017). This method was generally expressed as follows.

$$\frac{\mathrm{d}x}{\mathrm{d}t} = k_{\mathrm{RPM}}(1-x)\sqrt{1-\Psi(1-x)} \tag{12}$$

$$\Psi = \frac{4\pi L_0 (1 - \varepsilon_0)}{{S_0}^2} \tag{13}$$

here, Ψ represents the particle structure parameter, while S_0 , L_0 , and ε_0 denote the initial reaction surface, pore length, and initial porosity, respectively.

2.6.2. Homogeneous model (HM)

The HM assumed that the particle size remained unchanged throughout the gasification process, while the particle density underwent uniform changes (Zhang et al., 2015; Edreis et al., 2014). Furthermore, it postulated that the active sites were evenly distributed within the particle, and assigned a first-order reaction kinetics to the gasification process. Consequently, the representation of HM could be formulated as follows.

$$\frac{\mathrm{d}x}{\mathrm{d}t} = k_{\mathrm{HM}}(1-x) \tag{14}$$

2.6.3. Shrinking core model (SCM)

The SCM proposed that the surface of a spherical particle served as the primary location for gasification, with the gasification rate being influenced by the unreacted surface area or the remaining quantity of the particle (Edreis et al., 2017; Edreis et al.,

2018). When the chemical reaction was the rate-determining step, the reaction order was found to be 2/3. Consequently, the expression for SCM could be stated as follows.

$$\frac{\mathrm{d}x}{\mathrm{d}t} = k_{\text{SCM}} (1 - x)^{2/3} \tag{15}$$

3. Results and discussion

3.1. PC gasification reactivity

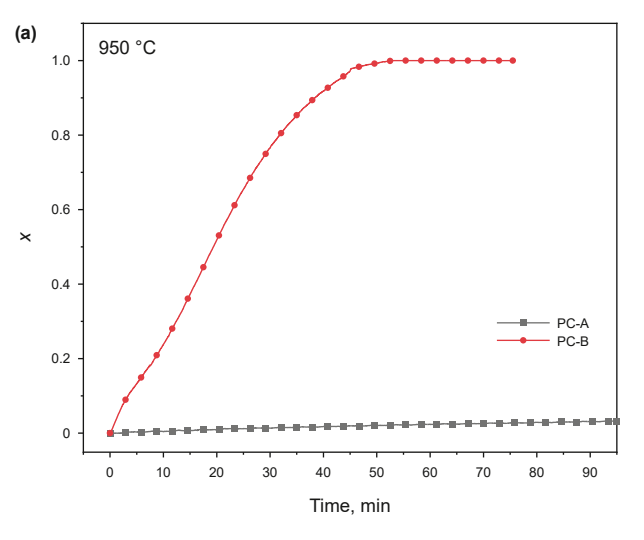
TGA was performed at 950 °C to investigate and compare the gasification reactivity of PC-A and PC-B. As illustrated in Fig. 1(a), the time-dependent changes in the conversion rate revealed a striking disparity in their reactivities. Notably, PC-B demonstrated significantly higher gasification reactivity, achieving full conversion within just 55 min. In contrast, PC-A exhibited a mere 2.3% conversion during the same timeframe.

To further explore the high-temperature gasification behavior of PC-A, supplementary experiments were conducted at elevated temperatures ranging from 1100 to 1300 °C, with results visualized in Fig. 1(b). The gasification reactivity of PC-A increased markedly with rising temperature. At 55 min, the conversion levels reached 14.9%, 33.3%, and 81.1% at respective temperatures of 1100, 1200, and 1300 °C, respectively. The pronounced difference in activity between these two types of PC might be attributed to their distinct compositional and structural features. A detailed examination of these factors is provided in Section 3.2.

3.2. PC characterization analysis

3.2.1. XRD analysis

The carbon microcrystalline structure within the materials plays a pivotal role in dictating their gasification performance (Li et al., 2014). Fig. 2 presents XRD patterns for PC-A and PC-B, highlighting characteristic (002) and (100) diffraction peaks occurring at approximately 25° and 43°, respectively. These peaks serve as indicators of the crystalline carbon content and the degree of aromatic carbon condensation (Zhou et al., 2023). Notably, PC-A



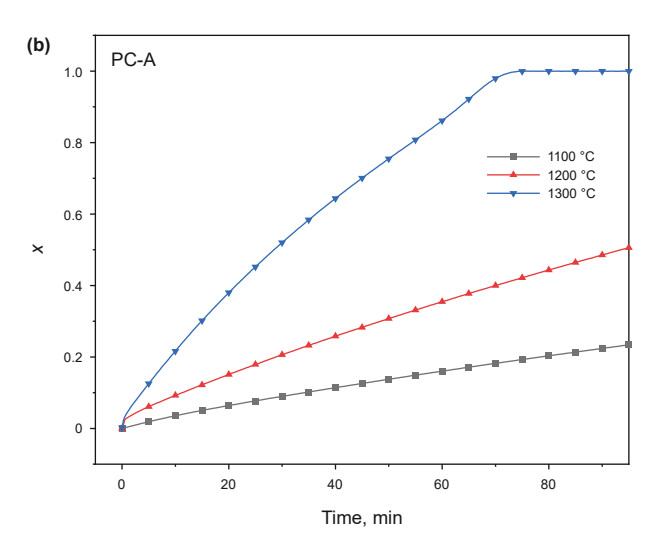


Fig. 1. (a) Carbon conversion rate versus time of PC-A and PC-B at 950 °C, (b) carbon conversion rate versus time of PC-A at 1100-1300 °C.

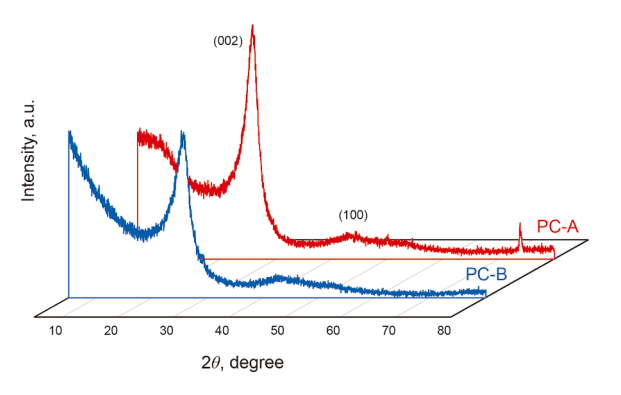


Fig. 2. XRD patterns of PC-A and PC-B.

manifested a more pronounced and sharper carbon (002) peak compared to PC-B, implying a higher degree of graphitization. This heightened graphitization contributes to PC-A's relatively lower reactivity during gasification.

To delve deeper into the microcrystalline structure, a meticulous peak fitting analysis was conducted over the range of $15^{\circ}-35^{\circ}$ for both PC samples, with results presented in Fig. 3. By applying Eqs. (7)–(11), the key microcrystalline parameters ($L_{\rm c}$, n, and CrI) were estimated and summarized in Table 3. The comparative analysis revealed that PC-B possessed lower values for $L_{\rm c}$, n, and CrI relative to PC-A. These findings suggested that PC-B featured a less densely packed aromatic carbon layer with a higher degree of disorder in its microcrystalline arrangement and a lesser degree of graphitization. Consequently, this structural characteristic enhanced the accessibility of active sites for gasification reactions, leading to PC-B's superior gasification activity.

3.2.2. FTIR analysis

The arrangement and abundance of functional groups in PC significantly influence its gasification reactivity, as demonstrated through FTIR spectroscopy analyses presented in Fig. 4. Seven distinct functional groups were identified: hydroxyl groups (–OH), aliphatic CH₃ and CH₂ groups, oxygen-containing functional groups (C=O and C-O), the C=C skeleton in benzene ring structures, and aromatic C-H bonds.

Notably, PC-B exhibited more pronounced absorption bands in the spectral ranges of 1000–1500, 1600–1800, and 3200–3650 cm⁻¹, indicative of enhanced concentrations of C=O, C-O, and -OH groups, respectively, compared to PC-A. These oxygen-rich functionalities acted as reactive sites, facilitating the

Table 3Carbon microcrystalline parameters and crystallinity index of PC-A and PC-B.

Sample	d ₀₀₂ , nm	L _c , nm	n	CrI, %
PC-A	0.3460	4.2735	12.35	50.50
PC-B	0.3474	4.1691	12.00	29.40

gasification process through bond cleavage and oxidation reactions, thereby enhancing PC-B's reactivity. Conversely, PC-A exhibited dominant absorption peaks within the 700–900 and 1500–1600 cm⁻¹ regions, suggesting a richer content of aromatic rings and higher aromaticity, which resulted in lower gasification activity.

To facilitate a semiquantitative assessment of functional groups, the infrared spectrum of PC was meticulously segmented into four key spectral regions (Dong et al., 2023; Li et al., 2022): hydroxyl structures (3250–3650 cm $^{-1}$), aliphatic structures (2800–3100 cm $^{-1}$), oxygen-containing structures (1000–1750 cm $^{-1}$), and aromatic structures (650–900 cm $^{-1}$). The peak fitting outcomes of PC samples for each region are depicted in Figs. 5 and 6, and quantitative parameters derived from these analyses are summarized in Table 4. The results highlighted that PC-A has higher values of $I_{\rm e}$ and $I_{\rm c}$, indicating a more condensed aromatic structure with a greater proportion of C–H aromatic bonds. This correlation with PC-A's lower activity implied that a higher degree of condensation and denser

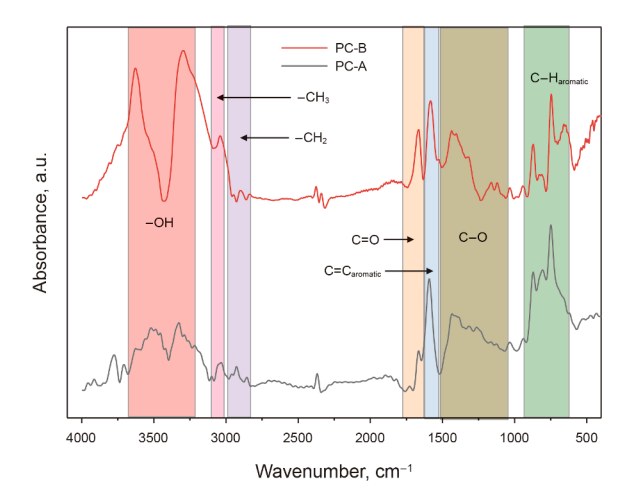
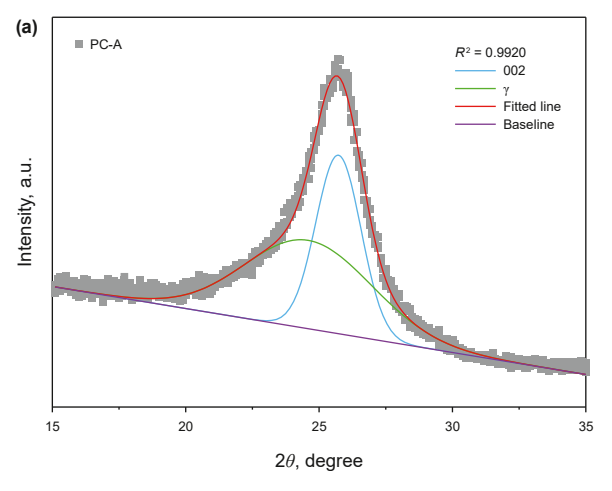


Fig. 4. FTIR spectroscopy of PC-A and PC-B.



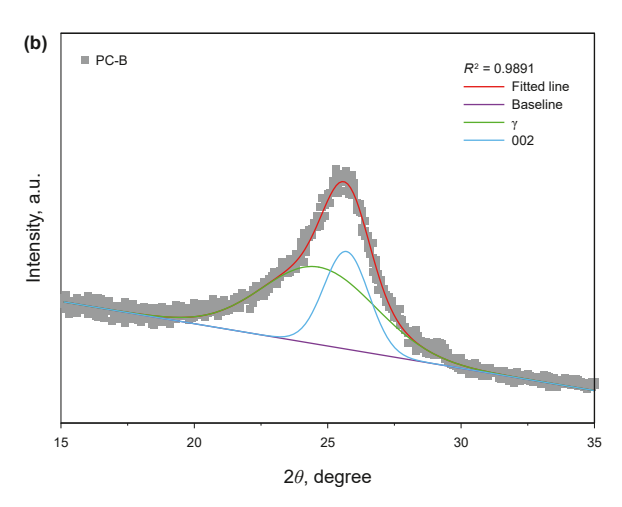


Fig. 3. (a) Curve fitting of XRD patterns for PC-A between 15° and 35°, (b) curve fitting of XRD patterns for PC-B between 15° and 35°.

aromatic structures hindered the gasification process by reducing the accessibility of reactive sites to gasifying agents. Interestingly, $I_{\rm a}$, typically considered the primary indicator for evaluating gasification activity, showed similar values for both PC-A and PC-B in this study. Consequently, it could be inferred that $I_{\rm e}$ and $I_{\rm c}$ were more closely correlated to gasification activity than $I_{\rm a}$ when assessing PC samples.

3.3. Effect of MT catalyst on PC gasification reactivity

To evaluate the effect of MT catalyst on the gasification performance of the PC samples, we designed experiments based on the distinct reaction characteristics of PC-A and PC-B. Catalyzed gasification tests were first conducted at 1100 °C with varying MT catalyst concentrations. As illustrated in Fig. 7(a), the addition of MT significantly improved PC-A's conversion rate compared to uncatalyzed conditions. However, increasing the MT content from 5 to 20 wt% did not result in substantial improvements in conversion efficiency.

Fig. 7(b) presents the gasification behavior of PC-A at a higher temperature of 1300 °C. PC-A achieved full carbon conversion within 75 min. Notably, the incremental benefits of adding MT catalyst gradually diminished, as all tested MT ratios exhibited similar carbon conversion rates. This observation underscored that at elevated temperatures, the thermal effect became the

predominant driver of gasification, overshadowing the influence of the catalyst. Temperature thus emerged as the paramount determinant of gasification activity at higher thermal levels.

Fig. 7(c) highlights the conversion process of PC-B during gasification at 1100 °C with the incorporation of MT catalyst. Strikingly, the data revealed a marked decline in the conversion rates upon introducing the MT catalyst. Without any catalyst, PC-B attained 100% conversion in just 13 min. Conversely, the presence of 20 wt% MT extended this time to 23 min, indicating a retardation in gasification reactivity. This adverse effect suggested potential incompatibility or negative interactions between the MT catalyst and PC-B, leading to reduced catalytic efficiency.

3.3.1. XRD analysis

Systematic experiments were performed to investigate the morphological transformations in carbon structure during PC gasification, with a particular emphasis on the influence of 5 wt% MT catalyst. By employing the isothermal gasification method at 1100 °C and targeting a 0.5 carbon conversion rate, we investigated the gasification residues of PC-A and PC-B, both with and without the catalyst.

Fig. 8 depicts the XRD patterns of four different PC gasification residues. The similarity in peak intensity for PC-A and PC-A \pm 5 wt% MT implied that the presence of MT catalyst did not significantly

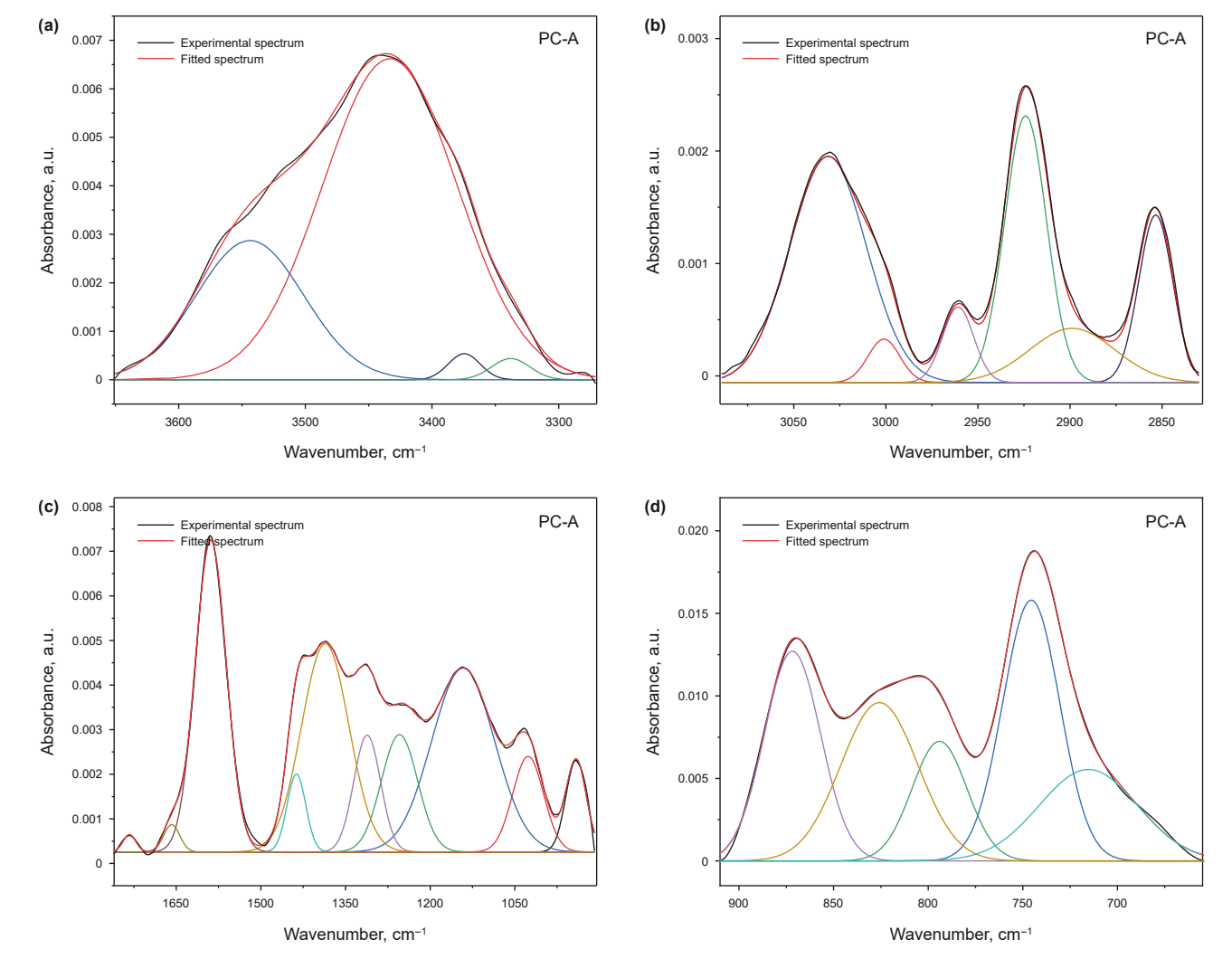


Fig. 5. Curve-fitting FTIR spectrum of PC-A: (a) absorbance bands of hydroxyl structures, (b) absorbance bands of aliphatic structures, (c) absorbance bands of oxygen-containing structures, (d) absorbance bands of aromatic structures.

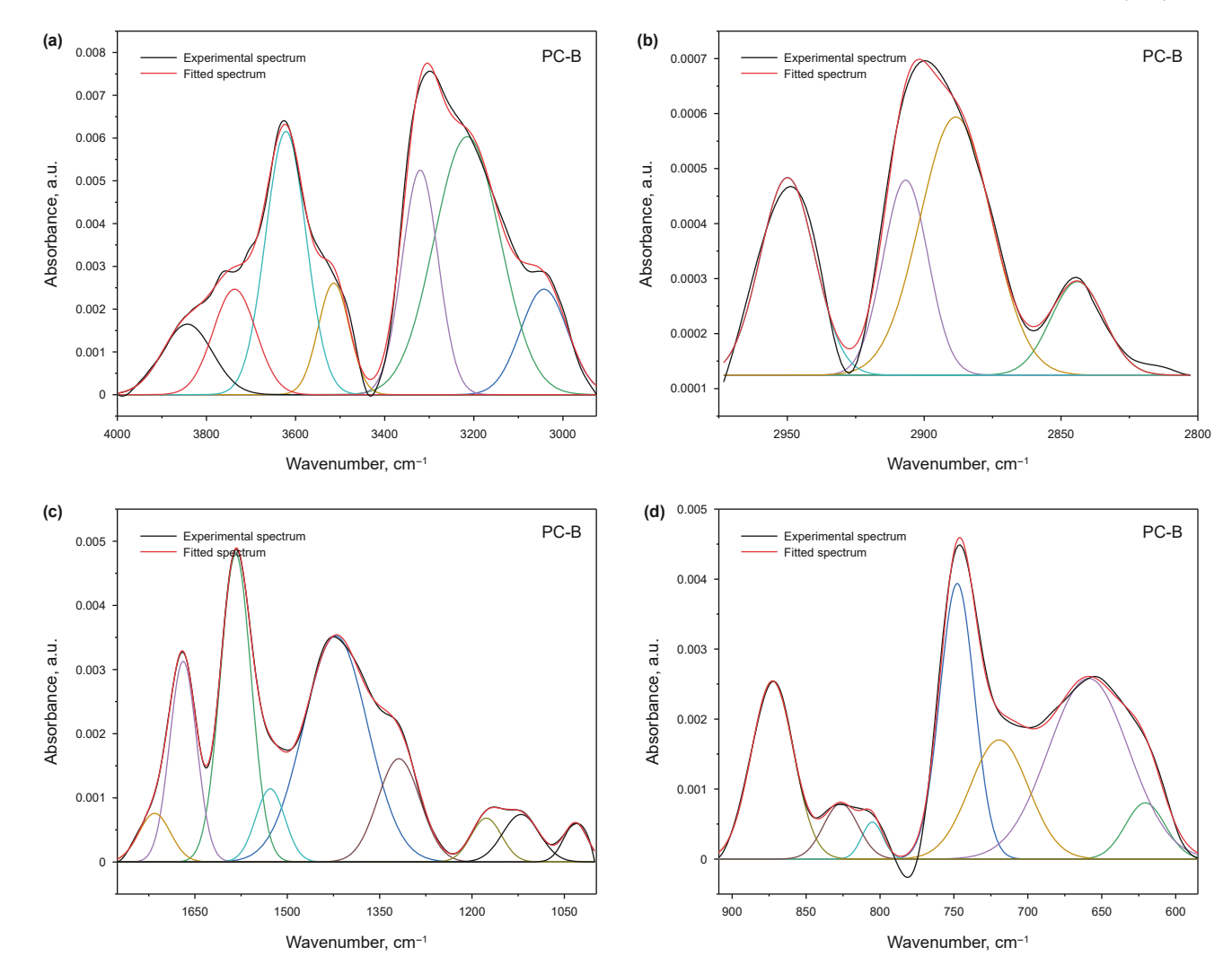


Fig. 6. Curve-fitting FTIR spectrum of PC-B: (a) absorbance bands of hydroxyl structures, (b) absorbance bands of aliphatic structures, (c) absorbance bands of oxygen-containing structures, (d) absorbance bands of aromatic structures.

alter the degree of graphitization in PC-A. Conversely, the increased intensity observed in PC-B with 5 wt% MT, relative to PC-B alone, indicated an unexpected effect of the MT catalyst. This increase suggested that the introduction of MT during PC-B's gasification promoted the formation of more amorphous carbon or smaller aromatic ring structures, deviating from the typical graphitic organization. This observation aligns with the previously discussed decrease in PC-B's gasification reactivity upon catalyst addition, as illustrated in Fig. 7(c).

In complement to the XRD analysis, Table 5 lists the peak fitting assessments on diffraction patterns observed between 15° and 35°. For PC-A, the addition of 5 wt% MT correlated with decreased values for L_c , n, and CrI, which indicated a microstructure that was less organized and more dispersed, characterized by lower levels of graphitization. On the contrary, PC-B + 5 wt% MT exhibited increased values in L_c , n, and CrI compared to PC-B alone. This

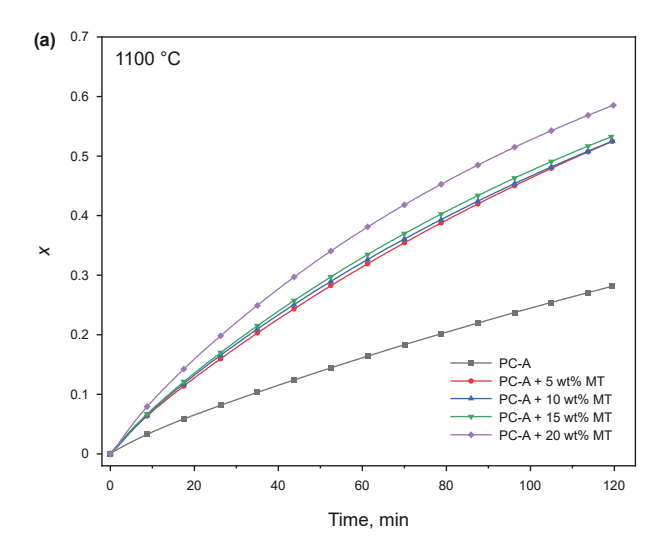
Table 4Fitting peak parameters of FT-IR spectrum for PC-A and PC-B.

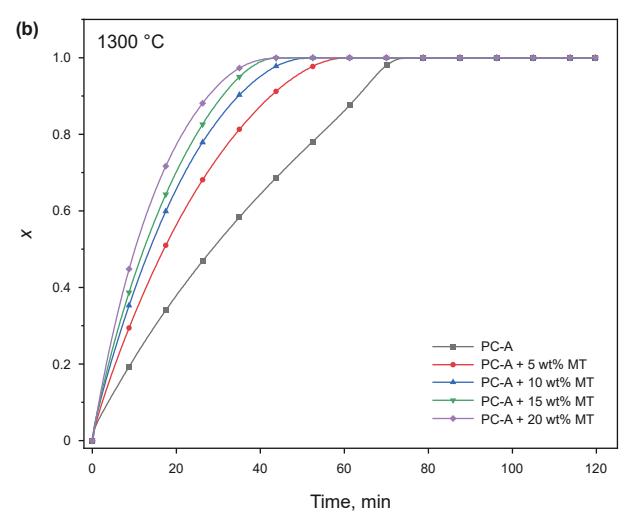
Sample	I _e	$I_{\mathbf{d}}$	I _c	I_{b}	Ia
PC-A	4.739	0.079	0.308	0.043	0.249
PC-B	0.817	0.150	0.045	0.161	0.251

further supported the notion that the MT catalyst promoted a more ordered carbon structure, which may have adversely affected PC-B's gasification reactivity.

In addition to providing insights into microcrystalline structures. XRD enables precise determination of crystalline mineral phases in carbonaceous materials. The interaction between the mineral constituents of the PC and MT catalyst plays a pivotal role in determining gasification reactivity. Fig. 9 presents the XRD patterns of PC gasification residues obtained at 1200 °C with different MT catalyst loadings. The mineralogical composition of PC-A ash with MT additives was predominantly composed of (Fe, Mg)₂SiO₄, MgO, CaAl₂Si₂O₈, Mg₂V₂O₇, (Ca,Fe,Mg)SiO₃, and CaSiO₃. MgO, recognized as an alkaline earth metal oxide, induced surface etching and generated interconnected channels within the carbon matrix. This catalytic penetration facilitated MgO diffusion into the PC's structural matrix, where it disrupted condensed aromatic configurations through the formation of Mg-enriched active sites (Yan et al., 2017; Jiao et al., 2020). These catalytic centers promoted C=C bond cleavage and initiated polycyclic aromatic hydrocarbon ring-opening reactions (Theofanidis et al., 2016), thereby substantially improving PC gasification efficiency.

In contrast, PC-B ash exhibited MgO interaction with Al₂O₃, forming the inert spinel phase MgAl₂O₄. This phase transformation





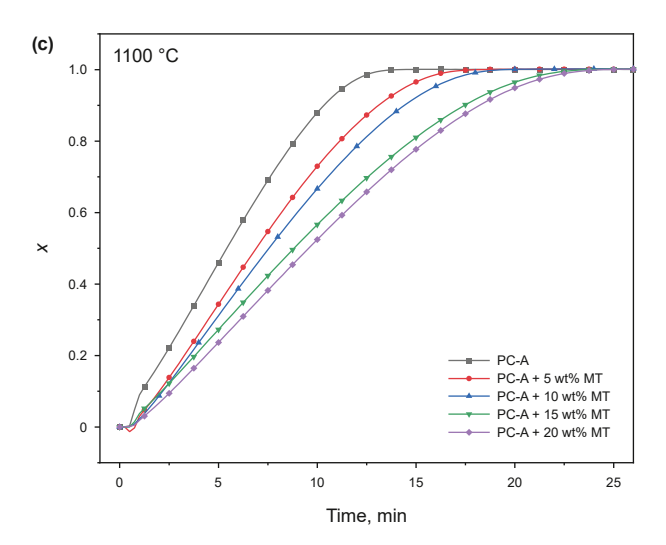


Fig. 7. (a) Effect of magnesium-rich catalyst on the gasification of PC-A at 1100 °C, (b) effect of magnesium-rich catalyst on the gasification of PC-A at 1300 °C, (c) effect of magnesium-rich catalyst on the gasification of PC-B at 1100 °C.

resulted in Mg component deactivation and consequent catalytic performance deterioration. The observed contrast in phase evolution provides a mechanistic explanation for the differential

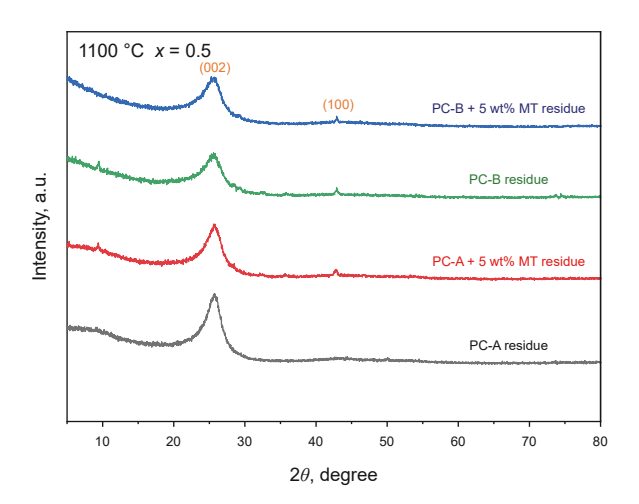


Fig. 8. XRD patterns of different PC residues with a x of 0.5 at 1100 °C.

catalytic behaviors between PC-A and PC-B systems during MT-assisted gasification. These findings collectively underscore the intricate relationships among catalyst composition, mineral phase transformations, structural modifications, and reaction kinetics, emphasizing the requirement for material-specific catalytic approaches in gasification optimization.

3.3.2. FTIR analysis

The FTIR spectroscopy analysis, as visualized in Fig. 10, provided a detailed insight into the modifications of functional group composition within the PC gasification residues. It is evident that some functional groups, including hydroxyl (–OH) and aliphatic CH₃ and CH₂ moieties, underwent significant diminution or complete disappearance. These changes were indicative of the extensive thermal degradation and chemical transformations that took place during the gasification process. The emergence of strong absorption bands in the 700–900 cm⁻¹ region indicated an increased aromaticity in the PC residues. This feature suggested the preservation or even enrichment of aromatic structures, despite the overall degradation of PC samples.

A notable observation was the variations in the intensity of C–H_{aromatic} absorption peaks between PC-A and PC-B residues in the presence of MT catalyst. For PC-A residues, the addition of the catalyst led to a decrease in peak intensity, suggesting a potential disruption or reduction in aromaticity. Conversely, for PC-B, the peak intensity increased, indicating the enhanced aromaticity. This divergence aligned with the previously reported impact of the MT catalyst on the gasification reactivity of the two PC samples, reinforcing the notion that the catalyst has differential effects depending on the specific structure of the PC material.

Furthermore, the presence of prominent C-O stretching and bending vibration peaks in the PC gasification residues suggested that, while the aromatic C-C bonds undergone cleavage, the reactive C(O) intermediates were formed on the PC surface. These intermediates were critical for promoting further gasification reactions and facilitating the release of gaseous products.

Table 5Carbon microcrystalline parameters and crystallinity index of PC-A and PC-B residues.

Sample	d_{002} , nm	$L_{\rm c}$, nm	L _a , nm	n	CrI, %
PC-A residue	0.3530	3.5735	1.6859	10.35	26.50
PC-A + 5 wt% MT residue	0.3536	2.9518	1.3653	10.14	25.72
PC-B residue	0.3645	2.7859	1.3144	10.01	20.13
PC-B + 5 wt% MT residue	0.3672	3.1691	1.7330	10.32	21.86

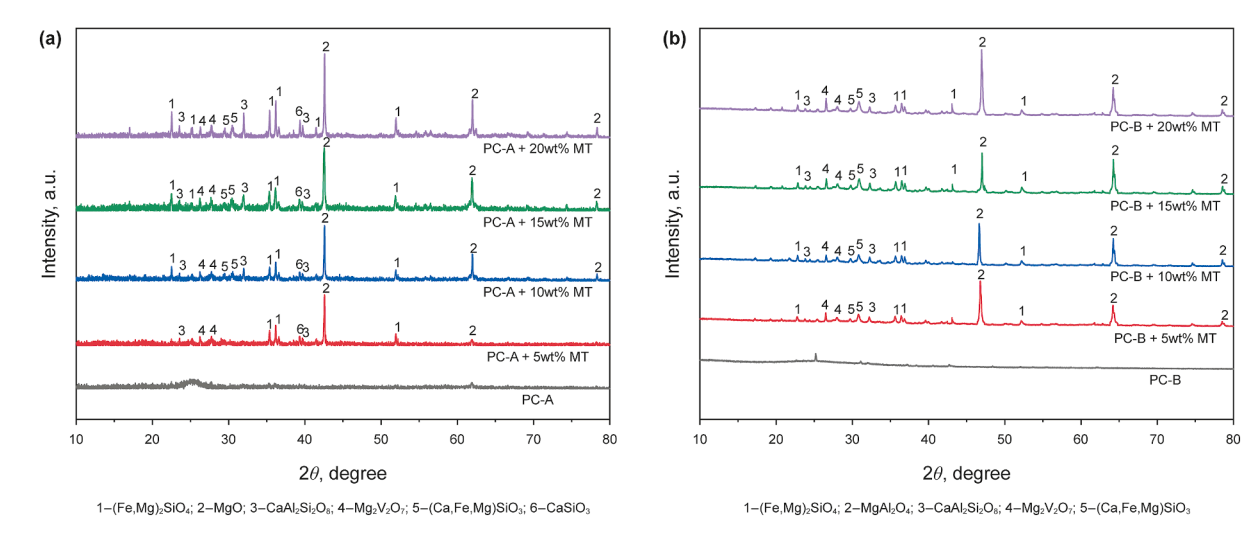


Fig. 9. (a) XRD patterns of different PC-A ashes at 1200 °C, (b) XRD patterns of different PC-A ashes at 1200 °C.

3.3.3. BET analysis

The reactivity of solid fuels during the gasification process is intricately linked to their internal structure, specifically the availability of active sites, which are significantly influenced by the specific surface area and pore characteristics (Nguven et al., 2022). BET tests were conducted on two PC samples and their gasification residues at various carbon conversion levels, and the corresponding results are summarized in Table 6.

The initially low specific surface area and pore volume of PC-A and PC-B suggested that surface area alone might not fully account

for their intrinsic reactivity towards gasification. However, as carbon conversion increased from 20% to 50% at a high temperature of 1100 °C, a significant enhancement in both specific surface area and pore volume was observed, accompanied by a reduction in average pore size. This trend indicates that the progressive degradation of PC during gasification generated more accessible surfaces and finer pores, potentially accelerating reaction kinetics.

For PC-A, the MT catalyst played a constructive role by significantly increasing its specific surface area and pore volume. This indicated that the catalyst effectively modified the structure of PC-

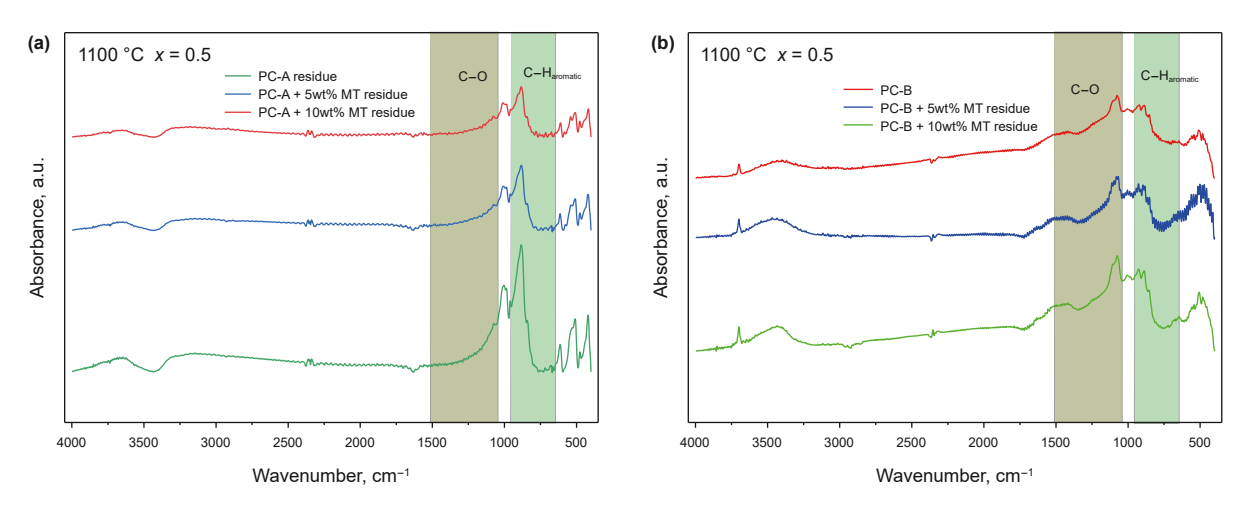


Fig. 10. (a) FTIR spectroscopy of different PC-A at 1100 °C with a x of 0.5, (b) FTIR spectroscopy of different PC-B at 1100 °C with a x of 0.5.

Table 6Specific surface area and pore volume of PC with different carbon conversions.

Sample	Carbon conversion	BET surface area, m ² /g	Total pore volume, cm ³ /g	Average pore size, nm
PC-A	x = 0	1.643	0.003	19.43
PC-A residue	x = 0.2	10.478	0.014	20.12
PC-A residue	x = 0.5	56.470	0.058	8.43
PC-A + 5 wt% MT residue	x = 0.2	14.125	0.020	22.43
PC-A + 5 wt% MT residue	x = 0.5	74.312	0.074	7.45
PC-B	x = 0	4.565	0.008	33.56
PC-B residue	x = 0.2	26.747	0.078	28.43
PC-B residue	x = 0.5	88.642	0.124	10.27
PC-B + 5 wt% MT residue	x = 0.2	20.412	0.056	27.36
PC-B + 5 wt% MT residue	x = 0.5	68.447	0.118	9.83

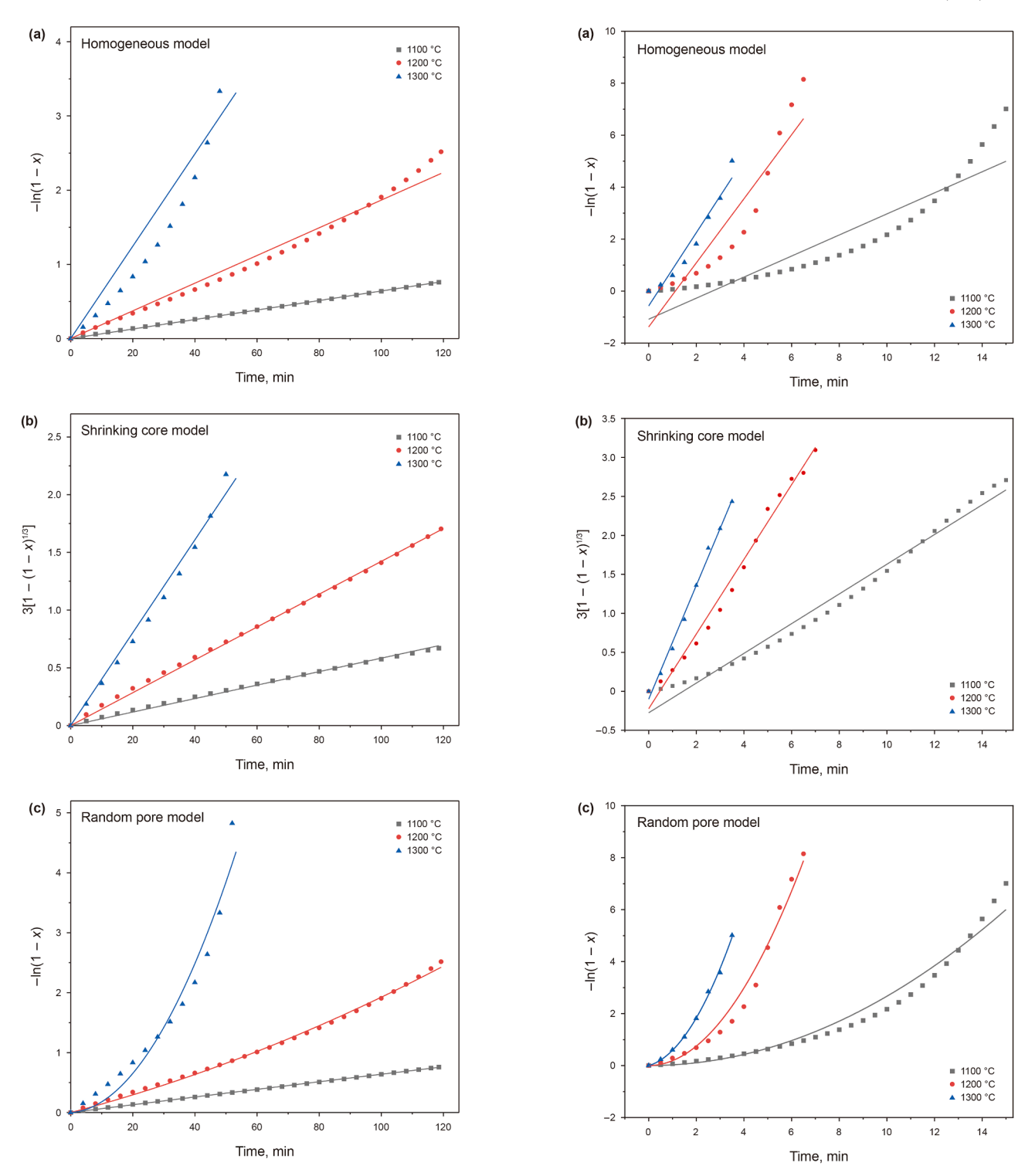


Fig. 11. Fitting curves for gasification reaction of PC-A \pm 5 wt% MT by three kinetic models.

A, fostering a more porous network that could enhance the mass transfer and catalytic activity, thus positively impacting gasification efficiency. Conversely, the influence of the MT catalyst on PC-B appeared to be detrimental to pore development, as evidenced by the reduced specific surface area and pore volume compared to the non-catalyzed PC-B residue. This discrepancy may stem from the

Fig. 12. Fitting curves for gasification reaction of PC-B \pm 5 wt% MT by three kinetic models.

physical obstruction of pores by catalyst particles, leading to pore blockage or collapse in the intense thermal environment. Such effects can limit the access of reactant gases to reactive sites, thereby hindering gasification efficiency.

These findings indicated that changes in specific surface area and pore volume were not the primary factors influencing the

Table 7Reaction rate constant and correlation coefficient of two samples.

Sample	T, °C	HM SCM		SCM	SCM		RPM	
		k, min ⁻¹	R ²	k, min ^{−1}	R^2	k, min ^{−1}	R^2	
PC-A + 5 wt% MT	1100	0.0283	0.9021	0.0272	0.9568	0.0250	0.9126	
	1200	0.0747	0.9143	0.0671	0.9952	0.0697	0.9452	
	1300	0.2465	0.9265	0.2259	0.9745	0.1944	0.9325	
PC-B + 5 wt% MT	1100	0.2335	0.9634	0.1682	0.9895	0.1337	0.9916	
	1200	0.6960	0.9266	0.4146	0.9866	0.2213	0.9865	
	1300	1.0573	0.9628	0.7720	0.9887	0.6157	0.9913	

catalytic gasification activity of PC when the MT catalyst was introduced.

3.4. PC gasification kinetic analysis

This investigation employed three unique kinetic models, HM, SCM, and RPM to determine the kinetic parameters governing the gasification processes of PC-A and PC-B samples, both catalyzed with a 5 wt% loading of MT catalyst. A comprehensive analysis of these models was conducted in Section 2.6. Figs. 11 and 12 graphically illustrate the model fits for the gasification of PC-A with 5 wt% MT and PC-B with 5 wt% MT, respectively. The outcomes of these fittings, including the reaction rate constants (k)and the linear correlation coefficients (R^2), are summarized in Table 7. Notably, all fitting curves achieved R^2 values exceeding 0.90, indicative of a strong correlation. Among the models, SCM exhibited the highest degree of fitting accuracy, with R^2 values exceeding 0.95, significantly outperforming both HM and PRM. This observation aligns with prior research (Li et al., 2024), which also reported the superior fitting performance of SCM over HM in the context of heavy oil residue gasification kinetics. According to the SCM calculations, the rate constants of PC-A+5 wt% MT and PC-B+5 wt% MT were 0.0272 and 0.1682 min⁻¹ at a temperature of 1100 °C, and escalated to 0.2259 and 0.7720 min⁻¹ at a heightened temperature of 1300 °C, respectively. These notable increases signified a marked acceleration in the gasification rate as temperature rises, emphasizing the substantial influence of thermal conditions on the reaction kinetics.

The Arrhenius equation establishes a relationship between the natural logarithm of the reaction rate constant ($\ln k$) and the inverse of the absolute temperature (1/T), facilitating the estimation of crucial kinetic parameters: the activation energy (E_a) and the pre-exponential factor (A). Fig. 13 illustrates the Arrhenius plot, depicting the concordance between the kinetic behavior of PC-A + 5 wt% MT and PC-B + 5 wt% MT during the gasification with respect to $\ln k$ and 1/T. This graphical representation confirms the adherence of the experimental gasification data to the expected linear trend as per the Arrhenius theory.

Deriving quantitative insights from this analysis, Table 8 summarizes the computed E_a and A for the gasification reactions of the two samples under the HM, SCM, and RPM frameworks. Specifically, for the SCM, the E_a of PC-A+5 wt% MT and PC-B+5 wt% MT were estimated to be 172.12 and 137.19 kJ/mol, respectively. Complementarily, the A of these two samples were calculated to be 4.62×10^4 and 2.86×10^4 min⁻¹, respectively. These values provide a quantitative foundation for understanding the energetic

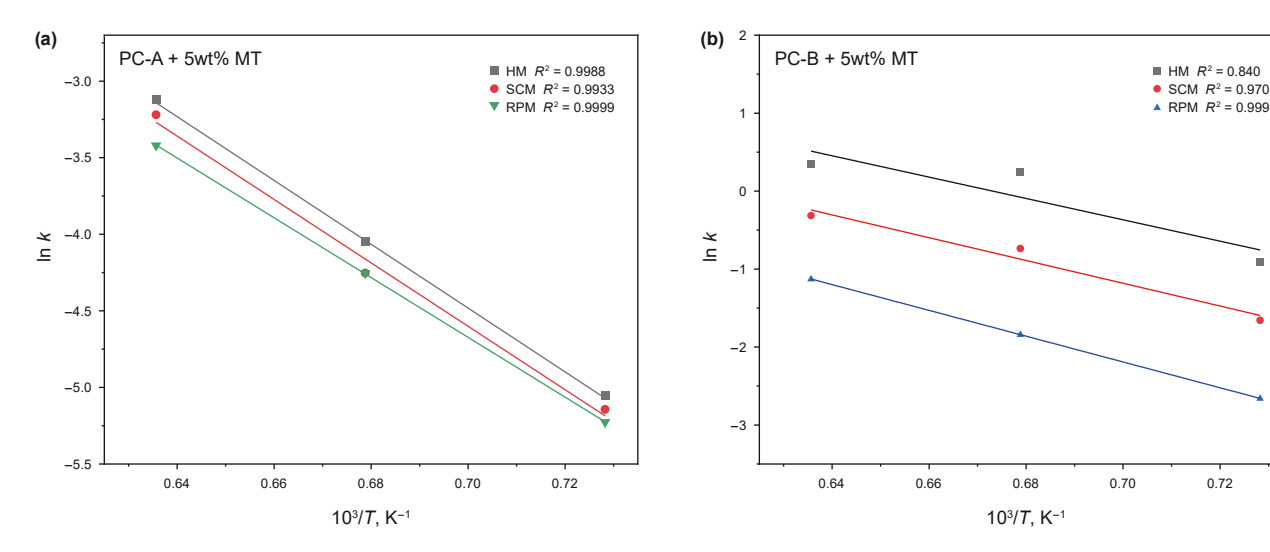


Fig. 13. Arrhenius equation plot for the kinetic parameters of (a) PC-A+5 wt% MT and (b) PC-B+5 wt% MT.

Table 8Kinetic parameters of PC-A+5 wt% MT and PC-B+5 wt% MT gasification.

Sample	$E_{\rm a}$, kJ/mol	E _a , kJ/mol			A, min ⁻¹		
	НМ	SCM	RPM	НМ	SCM	RPM	
PC-A+5 wt% MT PC-B+5 wt% MT	178.22 136.80	172.12 137.19	162.28 135.87	$5.39 \times 10^{4} \\ 4.08 \times 10^{4}$	$4.62 \times 10^{4} \\ 2.86 \times 10^{4}$	$\begin{array}{c} 2.06 \times 10^4 \\ 1.67 \times 10^4 \end{array}$	

parameters that govern the catalyzed gasification kinetics of the petroleum coke samples, offering critical insights into their reaction mechanisms.

4. Conclusions

This comprehensive study has meticulously analyzed the differences in gasification reactivity and carbon microstructural characteristics between two distinct types of petroleum coke, providing conclusive evidence of the divergent catalytic impacts of the MT catalyst on PC-A and PC-B gasification. These insights highlight the necessity for a more comprehensive approach to catalyst selection in petroleum coke catalytic gasification. It is essential not only to evaluate the cost-effectiveness of the catalyst but also to ensure that the selected catalyst can sustain its positive catalytic performance under operational conditions. The principal findings of the investigation can be drawn as follows.

- (1) PC-B exhibited significantly greater gasification reactivity compared to PC-A. XRD analyses revealed that PC-B's structure featured a less dense aromatic carbon layer, increased microcrystalline disorder, and a lower degree of graphitization, all factors contributing to its heightened reactivity.
- (2) The enriched content of oxygen-containing groups (C=O and C-O) in PC-B was attributed to its enhanced gasification activity, whereas PC-A was characterized by a predominance of aromatic rings and higher aromaticity. The indices of I_e and I_c showed a stronger correlation compared to I_a when evaluating the gasification performance of PC.
- (3) The MT catalyst exerted contrasting effects on the gasification of PC-A and PC-B due to differing evolutions in their carbon microstructures upon catalysis. Specifically, the introduction of MT catalyst in PC-B resulted in the formation of a more compact aromatic carbon layer, a better-organized microcrystalline structure, and an increase in graphitization. These outcomes contrasted sharply with the effects observed in PC-A, highlighting the catalyst's differential influence on each material's structural evolution.
- (4) SCM demonstrated superior fitting accuracy in comparison to HM and RPM when examining the kinetics of PC-A and PC-B catalytic gasification. Using SCM, the calculated activation energies for the gasification of PC-A + 5 wt% MT and PC-B + 5 wt% MT were determined to be 172.12 and 137.19 kJ/mol, respectively.

CRediT authorship contribution statement

Xian-Chao Du: Methodology, Formal analysis, Investigation. **Xiang Liu:** Software, Data curation, Resources. **Qian-Yun Liu:** Validation, Methodology, Supervision. **Bing Wang:** Writing – review & editing, Funding acquisition, Supervision.

Declaration of competing interest

The authors declare that they have no known competing financial interests or personal relationships that could have appeared to influence the work reported in this paper.

Acknowledgments

This work was supported by Natural Science Foundation of Henan Province (Nos. 242300421531), Doctor Program of Nanyang Normal University (No. 2022ZX006), National Natural Science

Cultivation Fund of Nanyang Normal University (No. 2023PY013), and Fundamental Research Program of Shanxi Province (No. 202303021222038).

References

- Alarcón, N., García, X., Centeno, M.A., et al., 2004. New effects during steam gasification of naphthalene: the synergy between CaO and MgO during the catalytic reaction. Appl. Catal. A-Gen. 267, 251–265. https://doi.org/10.1016/j.apcata.2004.03.010.
- Ban, Y.P., Liu, Q.S., Zhou, H.C., et al., 2019. Catalytic effect of representative calcium salts on the steam gasification of a Shengli lignite. Fuel 255, 115932. https:// doi.org/10.1016/j.fuel.2019.115832.
- Chen, Y.Y., Mastalerz, M., Schimmelmann, A., 2012. Characterization of chemical functional groups in macerals across different coal ranks via micro-FTIR spectroscopy. Int. J. Coal Geol. 104, 22–33. https://doi.org/10.1016/j.coal.2012.09.001.
- Dong, H.R., Liang, Y.H., Nie, J.H., et al., 2023a. Synthesis of forsterite with high strength and low acid solubility using magnesite tailings. Ceram. Int. 49, 13258–13264. https://doi.org/10.1016/j.ceramint.2023.01.066.
- Dong, M.F., Feng, L.L., Qin, B.T., 2023b. Characteristics of coal gasification with CO₂ after microwave irradiation based on TGA, FTIR and DFT theory. Energy 267, 126619. https://doi.org/10.1016/j.energy.2023.126619.
- Edreis, E.M.A., Li, X., Luo, G.Q., et al., 2018. Kinetic analyses and synergistic effects of CO₂ co-gasification of low sulfur petroleum coke and biomass wastes. Bioresour. Technol. 267, 54–62. https://doi.org/10.1016/j.biortech.2018.06.089.
- Edreis, E.M.A., Li, X., Xu, C.F., et al., 2017. Kinetic study and synergistic interactions on catalytic CO₂ gasification of Sudanese lower sulfur petroleum coke and sugar cane bagasse. J. Mater. Res. Technol. 6, 147–157. https://doi.org/10.1016/j.imrt.2016.09.001.
- Edreis, E.M.A., Luo, G.Q., Li, A.J., et al., 2014. Synergistic effects and kinetics thermal behavior of petroleum coke/biomass blends during H₂O co-gasification. Energy Convers. Manag. 79, 355–366. https://doi.org/10.1016/j.enconman.2013.12.043.
- Gao, Z., Hu, J., Guo, Z., et al., 2011. Study on CO₂ co-gasification characteristics and activation energy distribution of coal coke and biomass coke. Proc. CSEE. 31, 51–57. https://doi.org/10.13334/j.0258-8013.pcsee.2011.08.011.
- He, Q., Li, H., Wang, S., et al., 2022. Study on the effect and kinetics of coal liquefaction iron-based catalyst on coal coke gasification. J. Fuel Chem. Technol. 50, 1–9. https://doi.org/10.19906/j.cnki.JFCT.2021072.
- Jiao, W.H., Wang, Z.Q., Jiao, W.Y., et al., 2020. Influencing factors and reaction mechanism for catalytic CO₂ gasification of sawdust char using K-modified transition metal composite catalysts: experimental and DFT studies. Energy Convers. Manag. 208, 112522. https://doi.org/10.1016/j.enconman. 2020.112522.
- Li, J.Z., Wang, X.Y., Wang, B., et al., 2018. Investigation on the fates of vanadium and nickel during co-gasification of petroleum coke with biomass. Bioresour. Technol. 257, 47–53. https://doi.org/10.1016/j.biortech.2018.02.065.
- Li, J.Z., Wu, H.X., Zhang, Y.M., et al., 2024. Transformation behavior of potassium-containing minerals during co-gasification of petroleum coke and biomass. Fuel 355, 129492. https://doi.org/10.1016/j.fuel.2023.129492.
- Li, Q., Wang, X., Xin, Y., et al., 2014a. A unified intermediate and mechanism for soot combustion on potassium-supported oxides. Sci. Rep. 4, 4725. https://doi. org/10.1038/srep04725.
- Li, W., Pudasainee, D., Gupta, R., et al., 2022. The fate of char structure and active groups in petroleum coke gasification in a drop tube furnace. Fuel 310, 122438. https://doi.org/10.1016/j.fuel.2021.122438.
- Li, Y., Yang, H.P., Hu, J.H., et al., 2014b. Effect of catalysts on the reactivity and structure evolution of char in petroleum coke steam gasification. Fuel 117, 1174–1180. https://doi.org/10.1016/j.fuel.2013.08.066.
- Liang, R.Z., Tian, W., Yan, F.S., 2019. Effects of magnesium compounds on the gasification of petroleum coke. Petrol. Sci. Technol. 37, 135–145. https://doi.org/ 10.1080/10916466.2018.1517167.
- Linghu, R.X., Liu, Y.D., Zhang, Y.M., et al., 2019. Characterization of delayed coke and fluid coke gasification using blast furnace slag as a disposable catalyst. Energy Fuel. 33, 6734–6741. https://pubs.acs.org/doi/abs/10.1021/acs.energyfuels. 9b01173.
- Liu, M., Li, F.H., Liu, H.F., et al., 2021. Synergistic effect on co-gasification of chicken manure and petroleum coke: an investigation of sustainable waste management. Chem. Eng. J. 417, 128008. https://doi.org/10.1016/j.cej.2020.128008.
- Lopez-Gonzalez, D., Fernandez-Lopez, M., Valverde, J.L., et al., 2014. Gasification of lignocellulosic biomass char obtained from pyrolysis: kinetic and evolved gas analyses. Energy 71, 456–467. https://doi.org/10.1016/j.energy.2014.04.105.
- Lu, L., Sahajwalla, V., Kong, C., et al., 2001. Quantitative X-ray diffraction analysis and its application to various coals. Carbon 39, 1821–1833. https://doi.org/ 10.1016/S0008-6223(00)00318-3.
- Mei, Y.G., Wang, Z.Q., Fang, H.B., et al., 2017. Na-containing mineral transformation behaviors during Na₂CO₃-catalyzed CO₂ gasification of high-alumina coal. Energy Fuel. 31, 1235–1242. https://pubs.acs.org/doi/10.1021/acs.energyfuels. 6b02401
- Nguven, H.N., Khuong, D.A., Tran-Nguven, P.L., et al., 2022. Towards sustainable biomass gasification: evolution of bagasse char characteristics throughout gasification. Biomass Bioenergy 158, 106384. https://doi.org/10.1016/j. biombioe.2022.106384.

- Ouyang, P., Cui, D.M., Zhang, R., et al., 2020. Effect of potassium base composite catalyst on gasification performance of high sulfur petroleum coke. Acta Petrol. Sin. 36, 262–272. https://doi.org/10.3969/j.issn.1001-8719.2020.02.006.
- Theofanidis, S.A., Batchu, R., Galcita, V., et al., 2016. Carbon gasification from Fe-Ni catalysts after methane dry reforming. Appl. Catal. B Environ. 185, 42–55. https://doi.org/10.1016/j.apcatb.2015.12.006.
- Tian, W., Liang, R., Yan, F., 2019. Effects of MgCl₂ on the gasification kinetics of petroleum coke. Energy Sources, Part A 41, 746–760. https://doi.org/10.1080/ 15567036.2018.1520355.
- Wang, G.W., Zhang, J.L., Huang, X., et al., 2018. Co-gasification of petroleum cokebiomass blended char with steam at temperatures of 1173-1373K. Appl. Therm. Eng. 137, 678–688. https://doi.org/10.1016/j.applthermaleng.2018.04.026.
- Wang, G.W., Zhang, J.L., Zhang, G.H., et al., 2017. Experimental and kinetic studies on co-gasification of petroleum coke and biomass char blends. Energy 131, 27–40. https://doi.org/10.1016/j.energy.2017.05.023.
- Wang, J.X., Zhang, S.P., Xu, D., et al., 2022. Catalytic activity evaluation and deactivation progress of red mud/carbonaceous catalyst for efficient biomass gasification tar cracking. Fuel 323, 124278. https://doi.org/10.1016/j.fuel 2022.124278
- Wei, J.T., Guo, Q.H., Ding, L., et al., 2017. Synergy mechanism analysis of petroleum coke and municipal solid waste (MSW)-derived hydrochar co-gasification. Appl. Energy 206, 1354–1364. https://doi.org/10.1016/j.apenergy.2017.10.005.
- Wu, J.F., Montes, V., Virla, L.D., et al., 2018. Impacts of amount of chemical agent and addition of steam for activation of petroleum coke with KOH or NaOH. Fuel Process. Technol. 181, 53–60. https://doi.org/10.1016/j.fuproc.2018.09.018.
- Wu, Z.Q., Wang, S.Z., Luo, Z.Y., et al., 2017. Physico-chemical properties and gasification reactivity of co-pyrolysis char from different rank of coal blended with

- lignocellulosic biomass: effects of the cellulose. Bioresour. Technol. 235, 256–264. https://doi.org/10.1016/j.biortech.2017.03.121.
- Xu, B., Cao, Q.X., Kuang, D.Y., et al., 2020. Kinetics and mechanism of CO₂ gasification of coal catalyzed by Na₂CO₃, FeCO₃ and Na₂CO₃-FeCO₃. J. Energy Inst. 93, 922–933. https://doi.org/10.1016/j.joei.2019.08.004.
- Yan, S., Bi, J.C., Qu, X., 2017. The behavior of catalysts in hydrogasification of subbituminous coal in pressured fluidized bed. Appl. Energy 206, 406–412. https://doi.org/10.1016/j.apenergy.2017.08.189.
- Yu, J.Q., Gong, Y., Wei, J.T., et al., 2020. Promoting effect of biomass ash additives on high-temperature gasification of petroleum coke: reactivity and kinetic analysis. J. Energy Inst. 4, 1363–1372. https://doi.org/10.1016/j.joei.2019.12.006.
- Zhang, Y., Hara, S., Kajitani, S., et al., 2009. Modeling of catalytic gasification kinetics of coal char and carbon. Fuel 89, 152–157. https://doi.org/10.1016/j.fuel.2009.06.004.
- Zhang, Y.M., Yao, M.Q., Gao, S.Q., et al., 2015. Reactivity and kinetics for steam gasification of petroleum coke blended with black liquor in a micro fluidized bed. Appl. Energy 160, 820–828. https://doi.org/10.1016/j.apenergy. 2015.01.009.
- Zhou, L., Yang, Z.Y., Wei, D.J., et al., 2022. Application of Fe-based composite catalyst in biomass steam gasification to produce hydrogen rich gas. Front. Chem. 10, 882787. https://doi.org/10.3389/fchem.2022.882787.
- Zhou, T.H., Ge, L.C., Li, Q., et al., 2023. Combustion and gasification properties of petroleum coke and its pyrolytic semi-coke. Energy 266, 126414. https://doi.org/10.1016/j.energy.2022.126414.
- Zhu, H.Y., Shao, S.W., Guo, M.Z., et al., 2023. Engineering properties and sustainability evaluation of crushed low-grade magnesite mortars. J. Clean. Prod. 425, 138979. https://doi.org/10.1016/j.jclepro.2023.138979.